Particle fouling at hot reactor walls monitored *In situ* with a QCM-D and modeled with the frequency-domain lattice Boltzmann method

Diethelm Johannsmann [a,*], Judith Petri [a], Christian Leppin [a], Arne Langhoff [a], Hozan Ibrahim [b]

[a] *Institute of Physical Chemistry, Clausthal University of Technology, Arnold-Sommerfeld-Str. 4, 38678 Clausthal-Zellerfeld, Germany*
[b] *Institute of Applied Mechanics, Clausthal University of Technology, Adolph-Roemer-Str. 2A, 38678 Clausthal-Zellerfeld, Germany*

ARTICLE INFO

ABSTRACT

Fouling at a hot reactor wall during emulsion polymerization was studied in-situ with a quartz crystal microbalance with dissipation monitoring (QCM-D). Transient maxima in resonance bandwidth were observed, which are typically interpreted as the signature of a coupled resonance. However, the most common type of coupled resonances, the film resonance, cannot explain these observations, because the film resonance should occur first on the high overtones (on the overtones with small wavelength). In experiment, the low overtones reach the maximum first. The maximum in dissipation can be explained with the particulate nature of the sample. As the particles flatten out and merge, the height of the layer decreases and the surface becomes smoother. The decreasing height lets the layer go through the film resonance in reversed order. Also, the decreasing roughness lets the bandwidth decrease, unrelated to the film resonance. The argument is substantiated with a simulation based on the frequency-domain lattice Boltzmann method (FD-LBM). Apart from explaining the features seen in QCM experiments on particle fowling, this case study demonstrates the capabilities of FD-LBM.

Introduction

The quartz crystal microbalance (QCM) is among the convenient tools to monitor film thickness and changes thereof *in situ* [1]. The QCM has sub-monolayer sensitivity, in principle [2], but sensitivity is not necessarily its prime advantage compared to other techniques (such as surface plasmon resonance spectroscopy or ellipsometry [3]). Non-gravimetric effects often are as interesting as the gravimetrically determined thickness [4]. The latter statement applies to the QCM-D, where "D" stands for *Dissipation* monitoring.

Briefly, a QCM-D consists of a thickness-shear resonator that launches a shear wave into the sample. The shear wave decays within a few hundred nanometers, producing an oscillatory transverse stress at the resonator surface. The ratio of stress and strain (the load impedance, Z_L) governs the resonator's response to the presence of the sample. The QCM–D determines shifts in frequency, Δf, as well as shifts in half bandwidth, $\Delta \Gamma$. (The half bandwidth is proportional to the "dissipation factor" D. The two are related as $D = 2\Gamma/f_{res}$.) Δf and $\Delta \Gamma$ are determined on a number of different overtones (often $n = 3, 5, 7, 9$ with n the overtone order).

There are well-established algorithms for data analysis as long as the sample consists of a planar layer system [5–8]. These samples include rigid layers, analyzed with the Sauerbrey equation [9]. For soft layers, the data sets {$\Delta f/n$, $\Delta \Gamma/n$} can serve as input to an analysis leading to the layer's viscoelastic properties. For structured samples, however, the interpretation must rely on numerical simulations.

The experimental data underlying this work were obtained while studying heat-transfer fouling in emulsion polymerization [10,11]. The unwanted deposition of solid material on the reactor walls and the inside of the pipes (termed "fouling" in the following) is a prominent problem in emulsion polymerization. It currently necessitates emulsion polymerization to be carried out as a batch process. Tubular reactors running continuously have been demonstrated [12,13] but are not common practice. Techniques to quantify heat-transfer fouling have been reviewed in [14]. Studying heat-transfer fouling with a QCM is possible, but a way must be found to let the resonator be hotter than the reaction mixture. This is not usually the case. Fouling studies with a QCM outside of heat-transfer fouling are numerous. They have, for instance, concerned biofouling and its prevention [15]. Other publications have targeted latex dispersions [16], lime scale [17], microbial biofilms [18], and quality control in water treatment [19].

The method, by which the authors' group has recently adapted the

QCM to the study of heat-transfer fouling, is described in [20]. Briefly, a ring-shaped thermal pad heats the resonator from the back. A hole in the center of the pad avoids overdamping, where a compromise between small damping (large hole) and good heat transfer (small hole) must be found. Interestingly, a commercial QCM instrument has recently become available, which allows to study fowling at high temperatures and high pressures [21]. Huellemeier and coauthors have exploited this method to study the fowling of milk proteins [22,23] While this instrument emulates the conditions found in some important industrial processes, the resonator surface is at the same temperature as the reaction mixture. The deposits seen in [23] form at high temperature, but they do not amount to heat-transfer fouling in the narrow sense.

In [20], the QCM surface was indeed found to be covered with a polymer layer. Such layers are ubiquitous and are not a problem by themselves. In some instances, though, the layers continued to grow until the QCM's dynamic range was finally exceeded. Ex-situ observation after the experiment revealed thick deposits (millimeters and more). This is the undesired fouling pathway. Thick layers of this kind ultimately clog tubes and valves. Also, they lower the rate of heat transfer across the wall into the reaction mixture [24]. In the more interesting cases, thin polymer layers passivated the surface against further adsorption. The thickness of these layers corresponded to a few diameters of the latex spheres.

This work is not primarily concerned with the conditions leading to passivation, but rather with a side aspect, which is the occurrence of transient maxima in bandwidth. Such maxima are typically associated with a coupled resonance. At a coupled resonance, $\Delta\Gamma(t)$ goes through a maximum and the time derivative of $\Delta f(t)$ transiently becomes positive. The inflection point in $\Delta f(t)$ coincides with the maximum in $\Delta\Gamma(t)$. The maxima in Fig. 7A from [20] (see also section 3) might at first glance be interpreted as the consequence of a film resonance. A film resonance occurs when a planar film growing over time reaches a thickness of about a quarter of the wavelength of sound. In simple terms, the film is the analog of a vibrating reed, known from some musical instruments. The film is clamped at the bottom, while the stress-free top oscillates transversely with large amplitude. Films in a liquid are not strictly stress-free at the top, but the stress is small enough to allow for a coupled resonance.

The film resonance cannot explain these findings, though, because the different overtones reach the maximum in the wrong order. The high overtones (with small wavelength) should reach the film resonance first, but they do so last, in experiment. Presumably, the origin of the maximum in $\Delta\Gamma$ is not a film resonance, but rather the particulate nature of the sample. A more detailed explanation is sketched in Fig. 1. Two separate effects contribute: First, adsorbed spheres flatten out over time, which decreases the layer's effective thickness (Fig. 1B). Following this view, the sample goes through a film resonance on the low overtones first. Second, neighboring spheres merge and eventually form a continuous film (Fig. 1C). In the process, the scale of roughness of the interface between the layer and bulk decreases. Because the low overtones probe the larger spatial scales, the bandwidth decreases for those earlier than for the high overtones.

In order to make such an argument more quantitative, a model must be formulated, which relates the sample's structure to the data sets {$\Delta f/n$, $\Delta\Gamma/n$} as determined with the QCM. The authors are aware of two analytical approaches serving this purpose. Tarnapolsky et al. have put forward a set of equations based on a mechanical equivalent circuit, which represents soft spheres. This model is geared to bacterial adsorption [25]. It takes both translation and rotation into account. The Krakow group has proposed models, which include the hydrodynamic interaction between different spheres [26,27]. They describe this interaction with a screening function, which was originally developed to predict how particles adsorbed to a charged surface modify the streaming potential. As pointed out in [27], the model from [26] only matches the experimental QCM data, if there is a significant amount of slip at the contact.
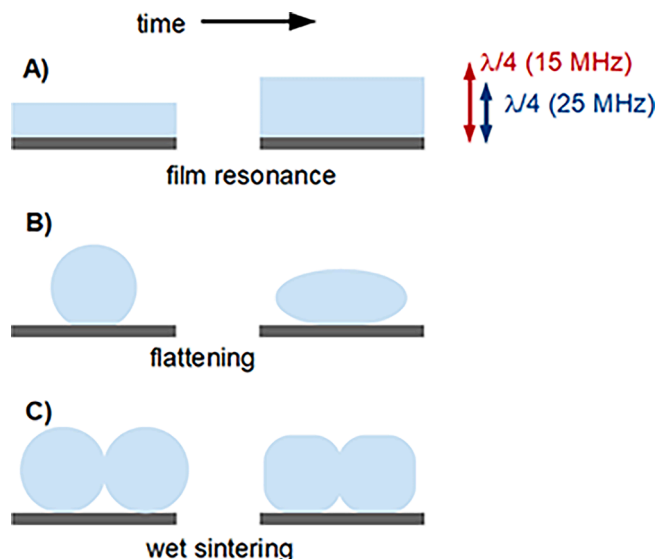

Fig. 1. When a film grows in thickness, the high overtones reach the condition of the film resonance first, followed by the low overtones (A). When adsorbed particles flatten out over time, the effective thickness decreases (B). Particle deformation and wet sintering eventually produce a homogeneous film (C). The scale of roughness of the layer surface decreases. Note the fundamental difference between case A, on the one hand, and cases B and C, on the other. In cases B and C, the geometric layer thickness *decreases* over time, due to compaction. This decrease is at the core of the working hypothesis underlying the simulations.

With regard to numerical simulations, any of the techniques available in computational fluid mechanics should be applicable, in principle. The authors' group has in the past employed the Finite Element Method (FEM), using COMSOL [28]. Ref. [28] demonstrated the principles, but could only be applied in 2D, not in 3D. Solving the incompressible Navier-Stokes equation with FEM poses some specific problems in 3D [29]. Xie et al. have used FEM in 3D to compute Δf and $\Delta\Gamma$ as induced by a contact with a particle in air [30]. A dry environment avoids the complications inherent to incompressible Navier-Stokes flow. As shown by Gillissen et al., the lattice Boltzmann method (LBM) is an option [31]. These calculations were demanding to the extent that parallelized code was needed. Ref. [31] is the most recent of a few publications treating QCM problems with LBM [32,33]. A hybrid technique using both numerical methods (the Finite Volume Method) and an advanced analytical formalism is reported in [34]. This work was specifically concerned with positive frequency shifts, which sometimes occur in experiments on adsorbed particles with a size larger than 1 µm.

Below, we employ a modification of the lattice Boltzmann method, described in [35] (see also section 4). The present work differs from the work by Gillissen et al. in two respects. First, a frequency-domain version of LBM (FD–LBM) is used. Second, an impedance boundary condition is applied at the interface with the bulk liquid. This allows to let the cell volume be much smaller than in [31], leading to an improved grid resolution. Separate from particle fowling, this work is meant to demonstrate the capabilities of FD–LBM. The main text focuses on the application of this method to particle fouling. Technical aspects of FD–LBM have been deferred to the supporting information (SI).

FD-LBM numerically solves the equations of viscoelasticity and hydrodynamics for a given geometry and given viscoelastic parameters. It computes the complex amplitude of the area-averaged oscillatory stress at the resonator surface, $\langle\sigma_S\rangle$, and uses this amplitude to infer the complex frequency shift, following the relation

$$\frac{\Delta f + i\Delta\Gamma}{f_0} = \frac{\Delta f + i(f_{res}\Delta D/2)}{f_0} = \frac{i}{\pi Z_q}\langle Z_L\rangle_{area} = \frac{i}{\pi Z_q}\frac{\langle\sigma_S\rangle_{area}}{u_S} \tag{1}$$

For the convenience of readers familiar with the dissipation factor, the shift in half bandwidth, $\Delta\Gamma$, was converted to ΔD in step 1. Z_L is the load impedance (a stress-velocity ratio). The amplitude of the transverse velocity of the resonator surface, u_S, is set to unity by the algorithm. f_0 is the frequency of the fundamental ($f_0 = 5$ MHz here), and $Z_q = 8.8 \cdot 10^6$ kg/(m²s) is the shear-wave impedance of the resonator plate. Of course, such simulations run forward, only. They require a hypothesis on the sample's structure and they test this hypothesis against experiment. They can never infer the structure of the sample from data sets {$\Delta f/n$, $\Delta\Gamma/n$}, because this problem would be underdetermined. In the case discussed below, the simulation supports the working hypothesis sketched in Fig. 1B and C. The test is not primarily based on quantitative agreement between simulation and experiment, but rather on certain characteristic features of the QCM response.

Critique of the interpretation of the maximum in bandwidth in terms of a coupled resonance

Among the features demonstrating non-gravimetric effects in QCM work is the film resonance. When a growing film reaches a thickness, d_f, of about $\lambda/4$ (with λ the wavelength of shear sound), the bandwidth goes through a maximum and $-\Delta f$ decreases (Fig. 2A). Naively interpreted with the Sauerbrey equation [9], decreasing $-\Delta f$ would indicate decreasing thickness.

The film resonance is one out of a few types of "coupled resonances". A peak in $\Delta\Gamma$ and a transient reversal of the time derivative of Δf occur, when the sample itself forms a resonator with a frequency comparable to the QCM's resonance frequency. Coupling between the two resonators leads to an enhanced rate of energy transfer between the main resonator and the sample, which then vibrates at large amplitude. The coupled resonance model predicts

$$\Delta f + i\Delta\Gamma = \frac{-iA}{\omega_{CR}^2 - \omega^2 + 2i\omega(2\pi\Gamma_{CR})} \qquad (2)$$

ω_{CR} and Γ_{CR} are the frequency and half bandwidth of the *Coupled Resonance*. A is a prefactor. Δf and $\Delta\Gamma$ as predicted by Eq. (2) are shown in Fig. 2A and B. In polar representation, coupled resonances produce circles or spirals [36].

A second type of coupled resonance (termed "particle resonance" in the following) is caused by surface-adsorbed particles [37,38]. The contact may be portrayed as a spring with some stiffness, κ_{eff}. The subscript "eff" indicates that both translation and rotation are involved

[25,39,40]. The resonance frequency of this mass-spring system, ω_{CR}, is given as $\omega_{CR} = (\kappa_{eff}/m_{eff})^{1/2}$ where m_{eff} is an effective mass. In principle, the maximum in $\Delta\Gamma$ seen in particle fouling experiments might be explained with a particle resonance. As the particle flattens out, the contact radius increases, which lets the contact stiffness increase. In consequence, ω_{CR} sweeps across the QCM's frequency range from low to high. The particle resonance explains the reversed overtone order but has shortcomings otherwise. For instance, the coupled resonance should let Δf increase simultaneously to the maximum in $\Delta\Gamma$ [3]. The situation is more complicated than what Fig. 2A and B suggest. Given these complications, Eq. (2) was not used for quantitative modeling. Rather, assumptions were made on the sample's structure as a function of time. These were used as input to an FD–LBM simulation. The simulation does find a maximum in $\Delta\Gamma$, but otherwise produces features, which cannot be explained with a coupled resonance, alone.

Materials and experimental

Instrumental

The experimental procedures have in detail been described in [20]. Impedance analysis was employed, using a vector network analyzer supplied by Makarov Instruments. The resonators (diameter of 25.4 mm, gold electrodes) were purchased from Quartz Pro, Stockholm. The resonator plates were heated from the back with a thermal pad (Kerafol 86/300, thickness of 1 mm). The reaction mixture was heated by the resonator, only. This experimental setting did not perfectly emulate the technical situation insofar as the polymerization mostly occurred at the resonator surface. None of the container's other walls were heated. The "nominal temperature" of 80 °C was the temperature of the resonator's holder. The resonator plate was mounted vertically, so that neither sedimentation nor creaming would drive coagulated material to the sensor surface. The stirrer was shaped as a propeller, creating a jet directed towards the resonator surface.

Chemicals

Polymerization was carried out as follows: Monomer in variable ratios of butyl acrylate (BA, Sigma Aldrich, purity $\geq$ 99 %) and methyl methacrylate (MMA, Acros Organics, purity $\geq$ 99 %) was added to ultra-pure water (resistivity $\geq$ 18.2MΩcm, generated by an arium 611VF reverse osmosis system, Sartorius) and the mixture was vigorously stirred to produce small monomer droplets. The suspension was purged
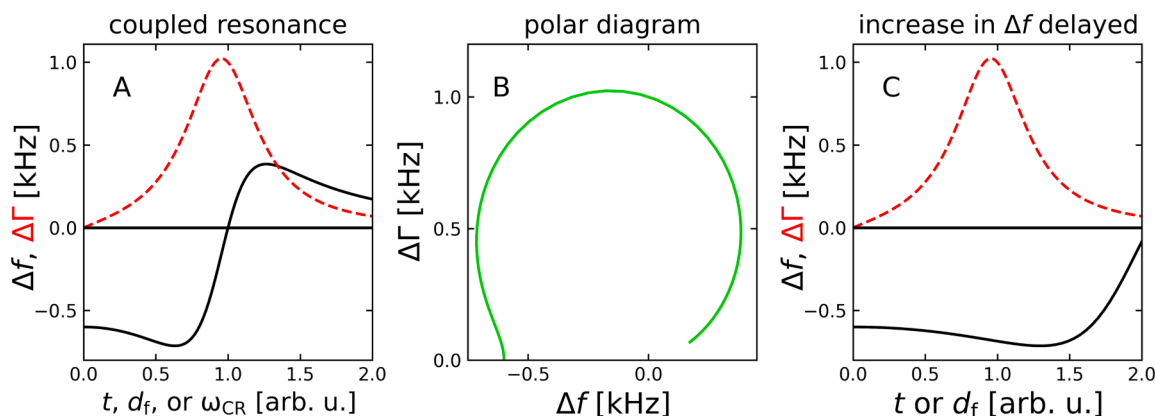
Fig. 2. The equations underlying the coupled resonance are the same as the equations underlying any other resonance. The role of the displacement in the conventional resonance is taken by the complex frequency shift, $\Delta f = \Delta f + i\Delta\Gamma$ (see Eq. (2)). Panel A shows the familiar resonance curve. The x–axis in this diagram is not the frequency of the QCM (which is almost constant on this scale), but rather the frequency of the coupled resonance, ω_{CR}, which sweeps across the frequency range of the QCM. For the case of the film resonance, ω_{CR} may – on a qualitative level – be replaced by thickness or time (assuming that the film grows over time). Polar diagrams as in panel B show circles or spirals. Panel C emphasizes that the experimental data do not quite agree with what is shown in panel A. Following the predictions of the coupled resonance model, the increase in Δf should occur at the same time as the maximum in $\Delta\Gamma$. In experiment, the increase in Δf occurs with a delay (if at all).

with nitrogen in order to remove oxygen. (Oxygen is a radical scavenger.) Acrylic acid (AA, Fluka, purity ≥ 99 %) was used as a co-monomer (1 % (w/w) of total monomer) to aid colloidal stability. A nonionic surfactant (Lutensol AT50, BASF) was added in a concentration of 7 % (w/w) relative to monomer, after purging with N_2. The ratio of monomer to water was chosen such that the final solids content was about 10 %. This low solids content avoids the formation of thick fowling layers. The reaction mixture was filled into the preheated chamber (80 °C) and allowed to equilibrate thermally. After a baseline had been acquired, the polymerization was started by adding 0.1 g of the initiator ($Na_2S_2O_8$, Merck, purity ≥ 99 %) dissolved in 1 mL of water. The total reaction volume after addition of the initiator was 14 mL. QCM data were taken in-line while polymerization proceeded.

The final diameter of the latex particles was determined with dynamic light scattering (DLS, Zetasizer Nano, Malvern Panalytical) as 100 ± 20 nm.

The fouling kinetics monitored in-line with a QCM-D

Fig. 3 shows data obtained on latexes with variable glass temperature, T_G. T_G is about 100 °C for poly(methyl methacrylate) (PMMA, Fig. 3A) and about −50 °C for poly(butyl acrylate) (PBA, Fig. 3D). The addition of the initiator is apparent in Fig. 3 in the form of small excursions in Δf and $\Delta\Gamma$ from the baseline at $t = 0$, caused by fluctuations in temperature. With a $\Delta f/n$-to-thickness ratio in the Sauerbrey regime of 5.7 Hz/nm ($f_0 = 5$ MHz, $\rho = 1$ g/cm^3), the deposition of a monolayer of such particles results in $-\Delta f/n \approx 500$ Hz. The final values of $-\Delta f/n$

are larger than 500 Hz in Fig. 3B and C. These latter deposits consist of multilayers. Multilayers were often observed for particles with intermediate T_G (~30 °C, the reaction temperature is higher than that). Particles with high T_G (PMMA) and low T_G (PBA) formed deposits consisting of about a monolayer of particles, which had flattened out. At least, this is what the frequency shift at the end of the experiment suggests ($-\Delta f/n \approx 300$ Hz). The modeling is limited to those samples, which consist of single layers of latex spheres. Theses samples are similar to what is shown in Fig. 1B and C.

Fig. 4 expands the range around the maximum in $\Delta\Gamma$ for the sample with the highest T_G (PMMA) and the sample with the lowest T_G (PBA). This graph is meant to emphasized that the different overtone orders to not go into the resonance sequentially from high to low, as predicted by the models based on the film resonance.

Simulation methods

The simulations are based on the frequency-domain lattice Boltzmann method (FD-LBM) as proposed by Shi and Sader [41]. Viggen has reported similar work [42] but the Viggen model does not fit the problem studied here to the same extent as the Shi-Sader model. The application of this method to the prediction of Δf and $\Delta\Gamma$ has been described in [35]. Briefly, the algorithm solves the frequency-domain version of the Stokes equation:

$$i\omega\rho(r)u(r) = \eta(r)\nabla^2 u(r) - \nabla p(r) \tag{3}$$

The properties of the sample are encoded in the functions $\rho(r)$ and $\eta(r)$. For simplicity, the density, ρ, was chosen as 1 g/cm^3 everywhere. FD-LBM allows for variable density (section 1.10 in the SI), but this possibility was not actually put to use in the simulation of particle fouling. Because the formalism is based on complex numbers, viscoelasticity is naturally included. The viscosity can be complex ($\eta_P = \eta_P' - i\eta_P''$). The subscript P in the following denotes a *Particle*. A
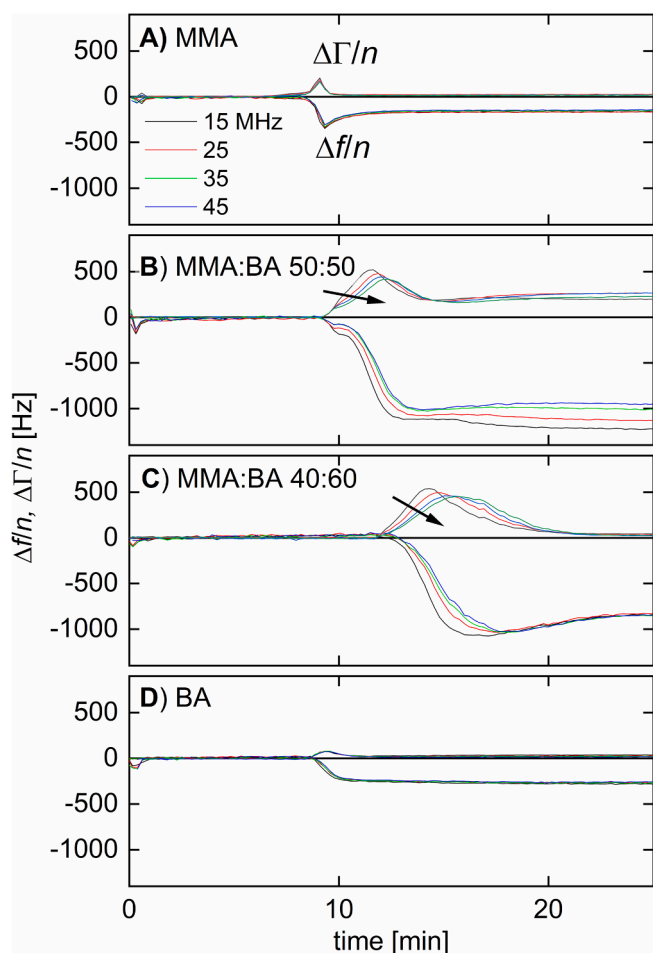

Fig. 3. Examples of QCM data traces obtained while studying heat-transfer fouling. As indicated by the arrows, the low overtones reach the maximum in bandwidth earlier than the high overtones.
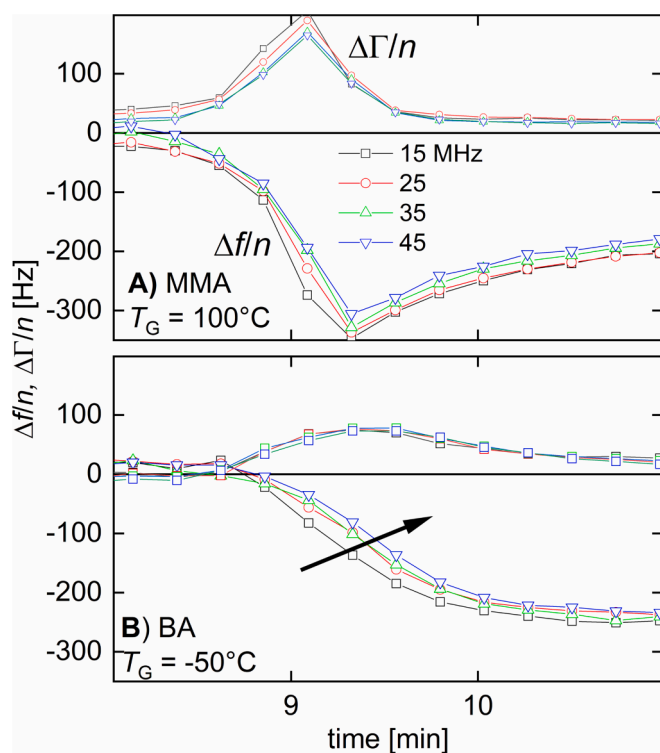

Fig. 4. Expanded data from Fig. 3A and D show the range around the maximum in $\Delta\Gamma$ in more detail. The high-T_G sample (top) differs from the low-T_G sample (bottom) in an increase in $\Delta f/n$ after the maximum in $\Delta\Gamma/n$. The arrow indicates increasing overtone order.

particle is a domain with $|\eta_P|$ larger than η_{Liq}. The loss tangent ($\tan(\delta_P) = \eta_p'/\eta_p''$) was varied, as well. η_{Liq} was chosen as 1 mPa s. The complex vector field $\mathbf{u}(\mathbf{r})$ in Eq. (3) is the amplitude of oscillation. The pressure, $p(\mathbf{r})$, is linked to the velocity field by the relation $p = -K/(i\omega)\nabla\cdot\mathbf{u}$. The modulus of compression, K, is discussed in section 1.3 of the SI. The liquid is almost incompressible.

In Eq. (3), $\mathbf{u}(\mathbf{r})$ is assumed as stationary. FD-LBM finds the stationary state by simulating a ring-in process (section 1.5 in the SI). The transverse movement of the resonator surface is turned on at $t = 0$. The resonator surface launches a shear wave into the medium. After a time corresponding to a few multiples of the characteristic time of the problem (which is $\tau_{\text{hyd}} = h^2/\nu$ with h the cell height and ν the kinematic viscosity), $\mathbf{u}(\mathbf{r})$ becomes stationary. If the spheres are predominantly elastic, one sometimes observes oscillations in the ring-in process, which require the ring-in process to run long enough to let those decay. Once stationarity has been reached, Δf and $\Delta\Gamma$ are inferred from the stress at the resonator surface, following the small-load approximation (Eq. (1)).

The current method of computation differs from [35] in the following regards:

- The entire code is written in Python, where the time-critical steps are accelerated with Numba [43]. Numba can also distribute the collision step (which can be parallelized easily) to the machine's different cores. Python code executing the core of the algorithm (ring-in, streaming, collision) is supplied in section 4 of the SI.
- Rather than treating a single particle, random positioning of a few particles is implemented. This avoids artifacts caused by interference effects between particles on a regular grid (section 8 in the SI to [35]). A single particle amounts to a periodic array of particles because of the periodic boundary conditions. Placing multiple particles in the unit cell alleviates the interference effects. The data points in Figs. 6 and 7 are obtained by averaging $\Delta f/n$ and $\Delta\Gamma/n$ over five such random configurations.
- The boundary condition at the upper edge of the simulation cell is based on a local impedance match rather than a match to the analytical solution in the bulk (section 1.6 in the SI).
- For the grid points located close to the boundary between domains, the relaxation rate in the collision step was chosen as the arithmetic mean of the relaxation rates in the two adjacent domains. The weight functions were the fractional volumes of the two domains in the respective cell as determined by Monte Carlo shooting (section 1.7 in the SI). This step reduces artifacts resulting from discretization (but does not completely eliminate them).

Limitations of FD-LBM are the following:

- When the boundary condition at the upper edge of the simulation volume is based on a local impedance match, it underestimates the amount of vertical flow at this interface.
- The grid resolution is the same in the entire simulation volume. A region, where improved resolution would be desirable, is the contact between the particle and the resonator surface.
- The computation time scales as the 5th power of grid resolution. A typical number of grid points is $n_x \times n_y \times n_z = 40 \times 40 \times 30$.
- FD-LBM produces systematic errors when the particle is much stiffer than the bulk liquid. When this is the case, the relaxation rate in the collision step is small and populations may traverse the entire domain with insignificant amounts of collision and relaxation. The problem can be alleviated with improved grid resolution, but improved grid resolution is expensive.
- At 30 MHz, a viscosity of 10 mPa s (10 times larger than the viscosity of the liquid) amounts to a shear modulus of 2 MPa. (Note that a Newtonian viscosity of 1 mPa s corresponds to $G'' \approx 0.2$ MPa at $f = 30$ MHz.) These are soft particles, but softness of this kind still realistically describes low-T_G materials. The difference between 2

MPa and 20 MPa would not much change the outcome of this simulation because the particles do not experience much internal shear. The difference would be of importance, if the dynamics of the sphere were governed by a narrow contact with the resonator surface, which experiences large local stress. Narrow contacts of this kind were avoided here.

Simulations were undertaken on cells containing three particles positioned randomly (Fig. 5A). $\Delta f/n$ and $\Delta\Gamma/n$ as reported in Figs. 6 and 7 are averages obtained from five such runs. The height of the particle center was set to $R(1–D_T)$ with R the sphere radius and D_T the degree of truncation ("truncation", for short, Fig. 5B). Truncation emulates flattening. The width of the truncated particle was slightly enlarged, so that the volume of the truncated particle (which is an oblate ellipse) equals the volume of the untruncated sphere.

Coverage is defined as $\pi R^2/L^2$ with L the width of the quadradic simulation box. A coverage of unity can only be achieved if neighboring spheres overlap, that is, if neighboring spheres merge by wet sintering.

The simulation allowed for an overlap between neighboring spheres of up to 1/3-rd of the sphere radius, which mimics wet sintering. In order to let the total volume of all particles remain constant in the presence over overlap, the volume contained in the overlapped region was determined by Monte-Carlo shooting and the entire assembly of spheres was slightly expanded vertically. The vertical expansion compensates for the volume in the overlapped regions. The particle radius was 50 nm (in agreement with experiment, radii determined by DLS). The grid resolution was $\Delta x = 6.25$ nm. The cell height was 200 nm. The absolute value of the sphere's viscosity, $|\eta_P|$, was 10 times larger than the (Newtonian) viscosity of the bulk liquid. The loss tangent was 0.3, 1.0, or 3.0. The shear modulus of the particle, G_P, is given as $G_P = i\omega\rho_P\eta_P$. Neither G_P' nor G_P'' was made to depend on frequency. Assuming both G_P' and G_P'' as constant amounts to a choice with regard to viscoelastic dispersion. Viscoelastic dispersion affects the comparison between overtones, in principle, but this comparison is unessential for the features discussed below. With these settings and a coverage of 0.5 (43 × 43 × 32 grid points), one ring-in requires about 0.2 min on a desktop computer with 6 cores. We also used clusters employing either 2 × AMD Epyc 7502 CPUs and 1024 GB RAM (64 physical cores, 128 logic cores) or 2 × AMD Epyc 7281 CPUs and 1024 GB RAM (32 physical cores, 64 logic cores). The RAM capacity was not fully exploited by this code, while the CPU resources were.
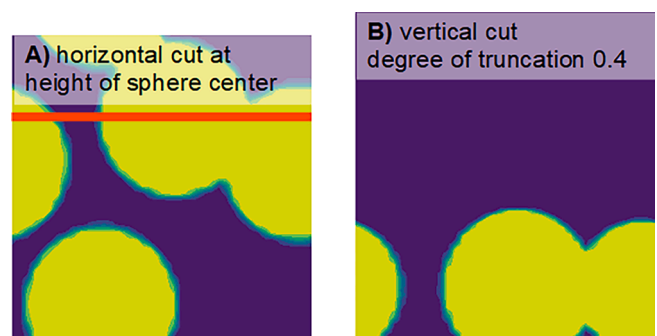

Fig. 5. A horizontal and a vertical cut through the simulation volume. The red line in panel A shows where the vertical cut for panel B was made. The coverage in this example is 0.67. Spheres were allowed to overlap by an amount equal to 1/6-th of the particle radius. The overlap emulates wet sintering. A closer look reveals the individual cells of the grid. Color encodes the local relaxation rate. At the boundaries between cells, the relaxation rate is an arithmetic mean of the relaxation rates in the adjacent domains (where the latter are calculated from Eq. S14 in the SI). (For interpretation of the references to color in this figure legend, the reader is referred to the web version of this article.)
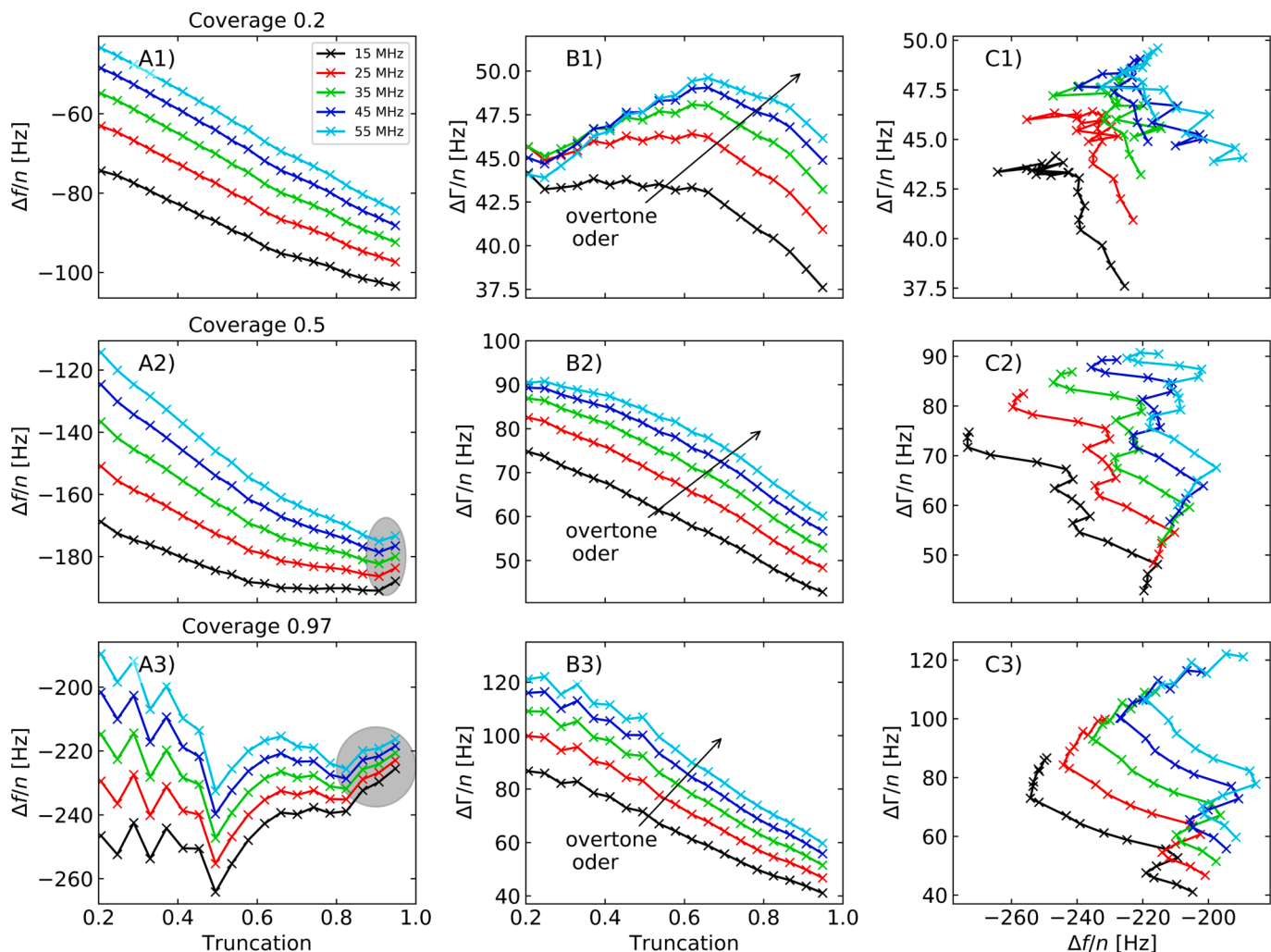
Fig. 6. Overtone-normalized shifts of frequency, $\Delta f/n$, (A1 – A3) and bandwidth, $\Delta \Gamma/n$, (B1 - B3) plotted versus truncation. The coverages are indicated above the panels on the left-hand side. The arrows indicate increasing overtone order. The grey ellipses in A2 and A3 indicate decreasing $-\Delta f/n$, caused by flattening. Panels C1 – C3 test for the coupled resonance. In a polar diagram, a coupled resonance produces a circle or a spiral. Whether increasing truncation drives a coupled resonance (which would amount to a particle resonance, see section 2) can be debated.

Simulation results

Figs. 6 and 7 show output from a typical simulation run. The loss tangent for this run was $\tan(\delta_P) = 1$. The maximum overlap amounted to 1/6th of the particle radius. These simulations comprise 5 overtones ($n = 3, 5, 7, 9, 11$), 20 degrees of truncation (linearly spaced between 0.2 and 1) and 20 coverages (linearly spaced between 0.1 and 1). Because these data suffer from discretization errors, the data shown in Fig. 6 all are moving averages over three neighboring values on the *x*-axis (which is the degree of truncation). Non-averaged data are shown in Fig. S9 in the SI. No averaging was needed on the coverage scale (Fig. 7).

Results from runs with other choices for the system parameters are provided in section 3 of the SI. These differ from Figs. 6 and 7 in the quantitative details, but not in the features underlying the interpretation.

Fig. 6A and B show $\Delta f/n$ and $\Delta \Gamma/n$ versus the degree of truncation for selected coverages. For low coverage, $-\Delta f/n$ *in*creases with truncation, which presumably is related to improved coupling between the sphere and the surface as sketched in Fig. 8A. At large coverage and large truncation, $-\Delta f/n$ *de*creases with truncation (grey ellipses in Fig. 6A2 and A3). Such a decrease is predicted by the mechanism sketched in Fig. 1B. The argument is reiterated in Fig. 8B. Fig. 8A invokes increasing contact stiffness (which may lead to a particle resonance), while Fig. 1B

does not.

As panels B1 – B3 in Fig. 6 show, the bandwidth mostly decreases with increasing truncation. Sometimes – but not always – there is a slight increase of $\Delta \Gamma/n$ with truncation at low truncation. In cases, where a maximum is seen (Fig. 6B1), the maximum shifts to higher truncation when the overtone order is increased (indicated by arrows). This result agrees with experiment and disagrees with the prediction from the film-resonance model.

Panels C1–C3 in Fig. 6 show polar plots ($\Delta \Gamma/n$ vs $\Delta f/n$, see also Fig. 2B). These plots test for the coupled resonance. A coupled resonance would produce a circle or spiral. There is a hint of a semicircle in Fig. 6C3. That is not proof for a coupled resonance, but does not strictly refute it, either.

Fig. 7 shows the same data as Fig. 6, but now versus coverage for selected truncations. There is an anomaly in $-\Delta f/n$ for the highest coverage in Fig. 7A1. It is related to overlap. We do not attribute much importance to this one data point.

As Fig. 7B shows, $\Delta \Gamma/n$ as a function of coverage sometimes displays a maximum. Similar maxima have occasionally been observed in experiments, where adsorbed polymers became more compact as the amount of adsorbed polymer increases. An example is reported in [44]. Increased density in these cases implies increased stiffness and decreased resonance bandwidth, in consequence. Maxima in resonance
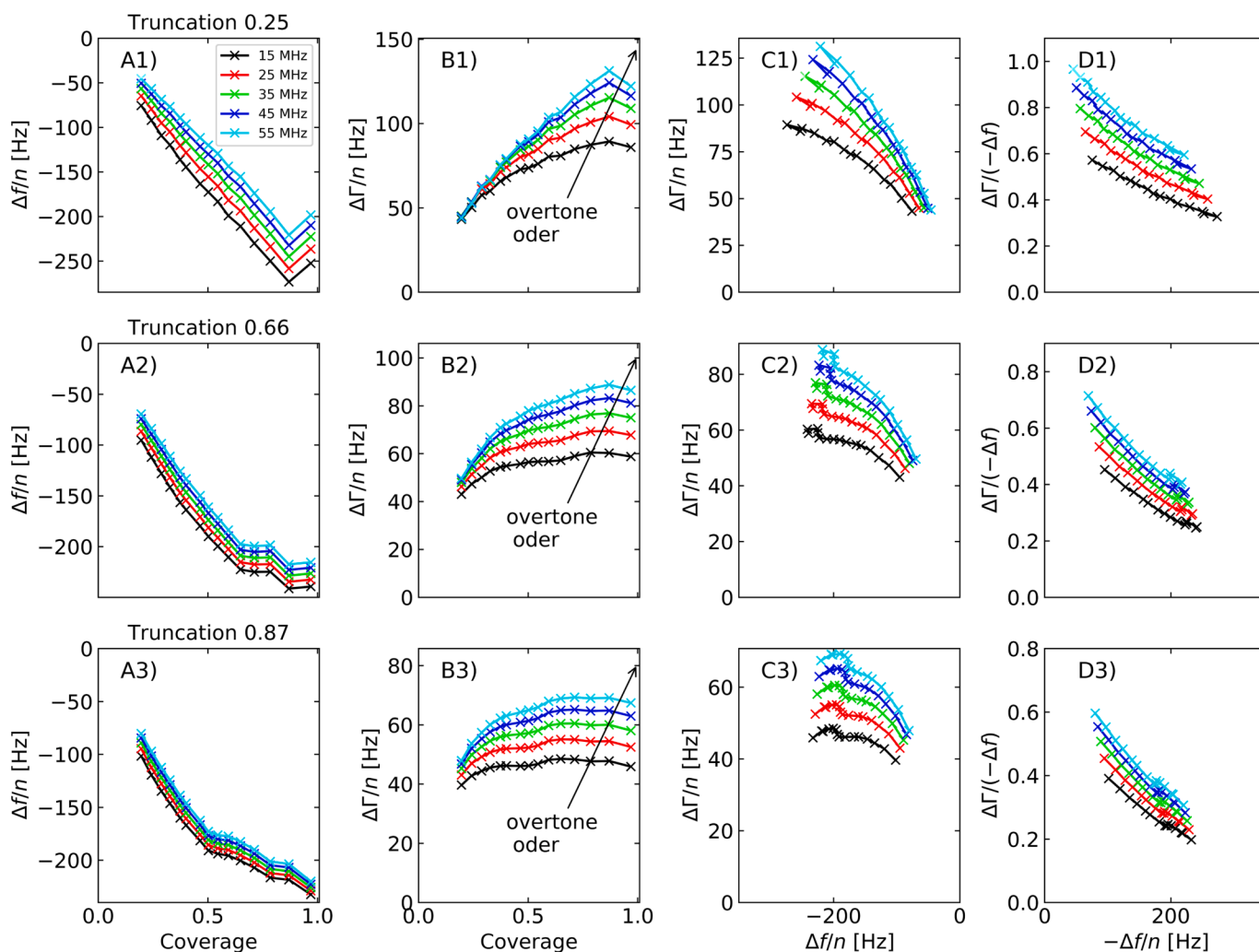
Fig. 7. Overtone-normalized shifts of frequency and bandwidth plotted versus coverage in A and B. The truncations are indicated above the panels on the left-hand side. Panels C and D test for the particle resonance and for the applicability of the $\Delta\Gamma/(-\Delta f)$–extrapolation scheme. For details see the main text.
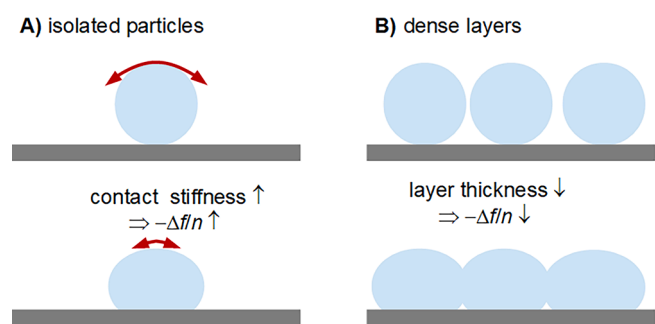

Fig. 8. When isolated particles flatten out, $-\Delta f/n$ increases due to an increased contact stiffness (A). However, when a dense layer of particles shrinks (flattens out), $-\Delta f/n$ decreases due to the decreased layer thickness (B). The latter effect explains what happens in the ranges covered by the grey ellipses in Fig. 6A2 and A3.

bandwidth have also been observed while adsorbing virus particles to a QCM surface [45]. These particles are rather stiff, internally. The decreased dissipation at high coverage in these cases can be attributed to the pattern of fluid flow around the particles. High coverage is linked to a decrease in effective roughness. In most models of roughness effects in QCM experiments, the scale of roughness is divided by the depth of penetration of the shear wave, δ [46]. δ is the intrinsic length scale of the

problem. The higher overtones feel small-scale roughness stronger than the low overtones because of their lower δ. The slight decrease in $\Delta\Gamma/n$, which is sometimes seen at high coverage, presumably goes back to this effect. With exception of one data point in Fig. 6A1, $-\Delta f/n$ never decreases with increasing coverage (Fig. 7A).

Fig. 7C (polar plots as in Fig. 6C) tests for a coupled resonance driven by increasing coverage. The plot does not show circles or semicircles. Fig. 7D tests for the applicability of the $\Delta\Gamma/\Delta f$–extrapolation scheme [35,47]. According to the extrapolation scheme, a plot of $\Delta\Gamma/(-\Delta f)$ vs $-\Delta f/n$ shows straight lines, which extrapolate to the same point on the x–axis for all overtones. The data follow this prediction reasonably well, but the agreement is less impressive than in [35].

Comparison with experiment

In the introduction, two separate mechanisms were proposed to explain the maximum in $\Delta\Gamma$, which were flattening and reduced roughness caused by wet sintering. Neither mechanism alone can explain the experimental data. Flattening leads to a decrease in bandwidth and in some cases to an increase in frequency. It rarely leads to an increase in bandwidth. Mostly, increased coverage lets both $-\Delta f/n$ and $\Delta\Gamma/n$ increase (as in many adsorption experiments). Occasionally, large coverage lets the bandwidth decrease slightly. It rarely lets $-\Delta f/n$ decrease. Only the combination of both mechanisms can explain what is seen in Fig. 4. Initially, increased coverage lets $-\Delta f/n$ and $\Delta\Gamma/n$

increase. The decrease in $\Delta\Gamma/n$ and the – occasional – decrease in $-\Delta f/n$ observed in a later stage are caused by flattening. This explanation does not invoke a coupled resonance.

To further address the possibility of a coupled resonance, Fig. 9 shows polar plots of the experimental data from Fig. 4. For PMMA (Fig. 9A), the polar diagram does show what might be viewed as a spiral. Possibly, the particle resonance plays a role in this case. For PBA (Fig. 9B), the polar diagram does not show such an indication of a spiral.

The findings from Fig. 4 can be fully explained without a particle resonance. The difference between PMMA and PBA in this explanation simply is in the time needed for flattening. This time is longer for PMMA, hence the decrease $-\Delta f/n$. A similar decrease exists for PBA, in principle, but is masked by the increase in coverage occurring in parallel.

This leaves the question of why strong maxima in bandwidth are observed for multilayers (Fig. 3B and C). A coupled resonance is difficult to understand for multilayers, but increasing coverage, followed by compaction appears plausible. This configuration is too complicated to be reproduced with FD-LBM, but compaction of a multilayer is similar to flattening of a monolayer.

It should be emphasized at this point that wet sintering (as observed here) is one out of numerous mechanisms, which can drive a compaction. The most prominent example for compaction at a substrate probably is coagulation dipping [48]. In coagulation dipping the substrate releases a coagulant (often Ca^{2+}-ions), which destabilizes the polymer dispersion, leading to the formation of a film. Compaction can also be induced electrochemically, as in cathodic electrodeposition [49]. FD-LBM will allow to interpret QCM-D experiments on compaction [50,51] in mechanistic detail.

Conclusions

The maxima in bandwidth observed in QCM experiments on heat-transfer fouling can be traced back to the particulate nature of the sample. Hard particles (PMMA) and soft particles (PBA) differ in their behavior insofar, as PMMA does show a decrease in $-\Delta f/n$ after the peak in $\Delta\Gamma/n$, while PBA does not. FD-LBM reproduces the features seen in experiment. Key to the explanation is a flattening of the adsorbed spheres over time. A particle resonance may play a role, but is not strictly required for the explanation.

This interpretation amounts to a statement on whether the fouling process should be viewed as reaction fouling [52,53] or particle fouling [54]. If the mechanisms sketched in Fig. 1 indeed underly the experimental findings, the maximum in $\Delta\Gamma$ is caused by particles, not by a planar film. Chemical reactions at the resonator surface are certainly expected, but they mostly affect the attachment of particles. Would they produce a planar film, they would lead to a film resonance, at variance with experiment.

CRediT authorship contribution statement

Diethelm Johannsmann: Conceptualization, Methodology, Software, Validation, Formal analysis, Resources, Data curation, Writing – original draft, Writing – review & editing, Visualization, Supervision, Project administration, Funding acquisition. **Judith Petri:** Methodology, Formal analysis, Data curation, Writing – review & editing. **Christian Leppin:** Methodology, Software, Validation, Formal analysis, Data curation, Writing – review & editing, Visualization. **Arne Langhoff:** Writing – review & editing, Supervision. **Hozan Ibrahim:** Software.

Declaration of Competing Interest

The authors declare that they have no known competing financial interests or personal relationships that could have appeared to influence the work reported in this paper.
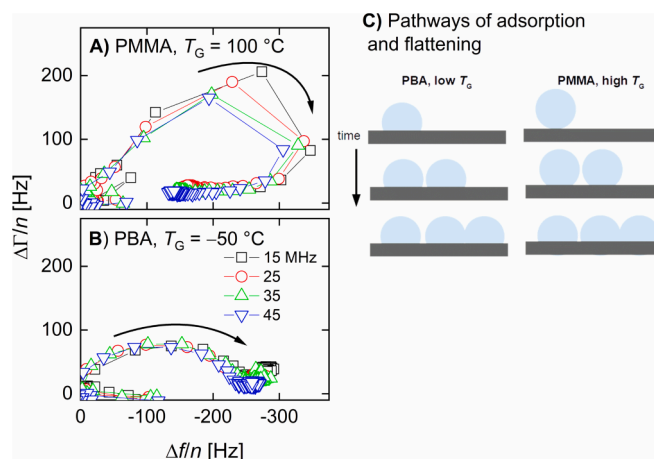

Fig. 9. Polar plots of the experimental data shown in Fig. 4. For the high-T_G sample (PMMA, panel A), a coupled resonance cannot be completely refuted. The arrows indicate increasing time. For the low-T_G sample (PBA, panel B), the data clearly do not lie on a circle or spiral. Panel C illustrates the difference between the two cases. $-\Delta f/n$ only decreases if flattening occurs *late* in the process. This is the case for the high-T_G material.

Data availability

Data will be made available on request.

Appendix A. Supplementary data

Supplementary data to this article can be found online at https://doi.org/10.1016/j.rinp.2023.106219.

References

[1] Steinem, C.; Janshoff, A., *Piezoeletric Sensors* Springer: Heidelberg, 2007.
[2] Lu C, Czanderna AW. Applications of Piezoelectric Quartz Crystal Microbalances. Amsterdam: Elsevier; 1984.
[3] Cooper MA. Label-free screening of bio-molecular interactions. Anal Bioanal Chem 2003;377(5):834–42.
[4] Lucklum R, Hauptmann P. Acoustic microsensors-the challenge behind microgravimetry. Anal Bioanal Chem 2006;384(3):667–82.
[5] Johannsmann D, Mathauer K, Wegner G, Knoll W. Viscoelastic properties of thin-films probed with a quartz-crystal resonator. Phys Rev B 1992;46(12):7808–15.
[6] Voinova MV, Rodahl M, Jonson M, Kasemo B. Viscoelastic acoustic response of layered polymer films at fluid-solid interfaces: continuum mechanics approach. Phys Scr 1999;59(5):391–6.
[7] Johannsmann D. Viscoelastic analysis of organic thin films on quartz resonators. Macromol Chem Phys 1999;200(3):501–16.
[8] Bandey HL, Martin SJ, Cernosek RW, Hillman AR. Modeling the responses of thickness-shear mode resonators under various loading conditions. Anal Chem 1999;71(11):2205–14.
[9] Sauerbrey G. Verwendung von schwingquarzen zur wägung dünner schichten und zur mikrowägung. Z Phys 1959;155(2):206–22.
[10] Urrutia J, Pena A, Asua JM. Reactor fouling by preformed latexes. Macromol React Eng 2017;11(1):1600043.
[11] Hohlen A, Augustin W, Scholl S. Quantification of polymer fouling on heat transfer surfaces during synthesis. Macromol React Eng 2019;14(1):1900035.
[12] Meuldijk J, Vanstrien CJG, Vandoormalen F, Thoenes D. A novel reactor for continuous emulsion polymerization. Chem Eng Sci 1992;47(9–11):2603–8.
[13] Pauer W. Reactor concepts for continuous emulsion polymerization. In: Pauer W, editor. Polymer Reaction Engineering of Dispersed Systems, Volume I. Cham: Springer International Publishing; 2017. p. 1–17.

[14] Wallhausser E, Hussein MA, Becker T. Detection methods of fouling in heat exchangers in the food industry. Food Control 2012;27(1):1–10.

[15] Alexander TE, Lozeau LD, Camesano TA. QCM-D characterization of time-dependence of bacterial adhesion. The Cell Surface 2019;5:100024.

[16] Kallio T, Kekkonen J, Stenius P. The formation of deposits on polymer surfaces in paper machine wet end. J Adhes 2004;80(10):933–69.

[17] Lu Y, Wei Q, Cheng Y, Ren XD, Wang H, Xie J. Investigation of scale inhibition mechanism by electrochemical quartz crystal microbalance. Int J Electrochem Sci 2021;16, (5):21057.

[18] Reipa V, Almeida J, Cole KD. Long-term monitoring of biofilm growth and disinfection using a quartz crystal microbalance and reflectance measurements. J Microbiol Methods 2006;66(3):449–59.

[19] Sprung C, Wahlisch D, Huttl R, Seidel J, Meyer A, Wolf G. Detection and monitoring of biofilm formation in water treatment systems by quartz crystal microbalance sensors. Water Sci Technol 2009;59(3):543–8.

[20] Böttcher A, Petri J, Langhoff A, Scholl S, Augustin W, Hohlen A, et al. Fouling pathways in emulsion polymerization differentiated with a quartz crystal microbalance (QCM) integrated into the reactor wall. Macromol React Eng 2022; 16:(2).

[21] https://www.biolinscientific.com/qsense/instrument/qsense-high-pressure.

[22] Huellemeier HA, Eren NM, Ortega-Anaya J, Jimenez-Flores R, Heldman DR. Application of quartz crystal microbalance with dissipation (QCM-D) to study low-temperature adsorption and fouling of milk fractions on stainless steel. Chem Eng Sci 2021;247.

[23] Huellemeier HA, Eren NM, Payne TD, Schultz ZD, Heldman DR. Monitoring and characterization of milk fouling on stainless steel using a high-pressure high-temperature quartz crystal microbalance with dissipation. Langmuir 2022. https://doi.org/10.1002/mren.202100045.

[24] Müller-Steinhagen H. Heat transfer fouling: 50 years after the kern and seaton modell. Heat Trans Eng 2011;32(1):1.

[25] Tarnapolsky A, Freger V. Modeling QCM-D response to deposition and attachment of microparticles and living cells. Anal Chem 2018;90(23):13960–8.

[26] Adamczyk Z, Sadowska M, Zeliszewska P. Applicability of QCM-D for quantitative measurements of nano- and microparticle deposition kinetics: theoretical modeling and experiments. Anal Chem 2020;92(22):15087–95.

[27] Adamczyk Z, Pomorska A, Sadowska M, Nattich-Rak MG, Morga M, Basinska T, et al. QCM-D investigations of anisotropic particle deposition kinetics: evidences of the hydrodynamic slip mechanisms. Anal Chem 2022;94(28):10234–44.

[28] Johannsmann D, Reviakine I, Rojas E, Gallego M. Effect of sample heterogeneity on the interpretation of QCM(-D) data: comparison of combined quartz crystal microbalance/atomic force microscopy measurements with finite element method modeling. Anal Chem 2008;80:8891.

[29] Valen-Sendstad K, Logg A, Mardal K-A, Narayanan H, Mortensen M. A comparison of finite element schemes for the incompressible Navier-Stokes equations. In: Logg A, K. A. M., G.N. Wells, , editors. Automated Solution of Differential Equations by the Finite Element Method, Vol. 84. Berlin Heidelberg: Springer:; 2011. p. 399–420.

[30] Xie X, Liu Y, Ye Y. FEM simulation and frequency shift calculation of a quartz crystal resonator adhered with soft micro-particulates considering contact deformation. IOP Conf Ser Mater Sci Eng 2020;892:012072.

[31] Gillissen JJJ, Jackman JA, Tabaei SR, Cho NJ. A numerical study on the effect of particle surface coverage on the quartz crystal microbalance response. Anal Chem 2018;90(3):2238.

[32] Gillissen JJJ, Tabaei SR, Jackman JA, Cho NJ. A model derived from hydrodynamic simulations for extracting the size of spherical particles from the quartz crystal microbalance. Analyst 2017;142(18):3370–9.

[33] Gillissen JJJ, Jackman JA, Tabaei SR, Yoon BK, Cho NJ. Quartz crystal microbalance model for quantitatively probing the deformation of adsorbed particles at low surface coverage. Anal Chem 2017;89(21):11711–8.

[34] Melendez M, Vazquez-Quesada A, Delgado-Buscalioni R. Load impedance of immersed layers on the quartz crystal microbalance: a comparison with colloidal suspensions of spheres. Langmuir 2020;36(31):9225–34.

[35] Gopalakrishna S, Langhoff A, Brenner G, Johannsmann D. Soft viscoelastic particles in contact with a quartz crystal microbalance (QCM): a frequency-domain lattice boltzmann simulation. Anal Chem 2021;93(29):10229–35.

[36] Olsson ALJ, van der Mei HC, Johannsmann D, Busscher HJ, Sharma PK. Probing colloid-substratum contact stiffness by acoustic sensing in a liquid phase. Anal Chem 2012;84(10):4504–12.

[37] Pomorska A, Shchukin D, Hammond R, Cooper MA, Grundmeier G, Johannsmann D. Positive frequency shifts observed upon adsorbing micron-sized solid objects to a quartz crystal microbalance from the liquid phase. Anal Chem 2010;82(6):2237–42.

[38] Dybwad GL. A sensitive new method for the determination of adhesive bonding between a particle and a substrate. J Appl Phys 1985;58(7):2789–90.

[39] Section 6.2 in, Johannsmann D, Langhoff A, Leppin C. Studying soft interfaces with shear waves: principles and applications of the quartz crystal microbalance (QCM). Sensors 2021;21:3490.

[40] Johannsmann D. Towards vibrational spectroscopy on surface-attached colloids performed with a quartz crystal microbalance. Sens Bio-Sens Res 2016;11:86–93.

[41] Shi Y, Sader JE. Lattice boltzmann method for oscillatory stokes flow with applications to micro- and nanodevices. Phys Rev E 2010;81(3):036706.

[42] Viggen EM. Viscously damped acoustic waves with the lattice Boltzmann method. Philos Trans R Soc A-Mathemat Phys Eng Sci 1944;2017(369):2246–54.

[43] https://numba.pydata.org/, accessed on 07.09.2022.

[44] Slavin S, Soeriyadi AH, Voorhaar L, Whittaker MR, Becer CR, Boyer C, et al. Adsorption behaviour of sulfur containing polymers to gold surfaces using QCM-D. Soft Matter 2012;8(1):118–28.

[45] Reviakine I, Johannsmann D, Richter RP. Hearing what you cannot see and visualizing what you hear: interpreting quartz crystal microbalance data from solvated interfaces. Anal Chem 2011;83(23):8838–48.

[46] Daikhin L, Gileadi E, Katz G, Tsionsky V, Urbakh M, Zagidulin D. Influence of roughness on the admittance of the quartz crystal microbalance immersed in liquids. Anal Chem 2002;74(3):554–61.

[47] Tellechea E, Johannsmann D, Steinmetz NF, Richter RP, Reviakine I. Model-independent analysis of QCM data on colloidal particle adsorption. Langmuir 2009; 25(9):5177–84.

[48] Groves R, Welche P, Routh AF. The coagulant dipping process of nitrile latex: investigations of former motion effects and coagulant loss into the dipping compound. Soft Matter 2022. https://doi.org/10.1039/d2sm01201d.

[49] Liu ZL, Onay H, Guo FZ, Lv QC, Sudholter EJR. Real-time monitoring of electrochemically induced calcium carbonate depositions: kinetics and mechanisms. Electrochim Acta 2021;370.

[50] Liu ZL, Hedayati P, Ghatkesar MK, Sun WC, Onay H, Groenendijk D, et al. Reducing anionic surfactant adsorption using polyacrylate as sacrificial agent investigated by QCM-D. J Colloid Interface Sci 2021;585:1–11.

[51] Zhitomirsky, I., Cathodic electrodeposition of ceramic and organoceramic materials. Fundamental aspects. Advances in Colloid and Interface Science 2002, 97, (1-3), 279-317.

[52] Watkinson AP. Chemical reaction fouling of organic fluids. Chem Eng Technol 1992;15:82–90.

[53] Panchal, C. B., Watkinson A. P. Chemical Reaction Fouling for Single-Phase Heat Transfer. ASME/AIChE National Heat Transfer Conference, August, Atlanta (1993).

[54] Henry C, Minier JP, Lefevre G. Towards a description of particulate fouling: From single particle deposition to clogging. Adv Colloid Interface Sci 2012;185:34–76.